catalysts

MDPI

Article

Modification of $NiSe_2$ Nanoparticles by ZIF-8-Derived NC for Boosting H_2O_2 Production from Electrochemical Oxygen Reduction in Acidic Media

Qiaoting Cheng, Hu Ding, Lang Chen, Jiatong Dong, Hao Yu, Shen Yan and Hua Wang *

Key Laboratory for Green Chemical Technology of Ministry of Education, Collaborative Innovation Center of Chemical Science and Engineering, School of Chemical Engineering and Technology, Tianjin University, Tianjin 300072, China; chengqiaoting163@163.com (Q.C.); dh13646462732@163.com (H.D.); chenlang@tju.edu.cn (L.C.); 2021207183@tju.edu.cn (J.D.); yuduohao2000@163.com (H.Y.); yan_shen@tju.edu.cn (S.Y.)

* Correspondence: tjuwanghua@tju.edu.cn

Abstract: The two-electron oxygen reduction reaction ($2e^-$ ORR) has emerged as an attractive alternative for H_2O_2 production. Developing efficient earth-abundant transition metal electrocatalysts and reaction mechanism exploration for H_2O_2 production are important but remain challenging. Herein, a nitrogen-doped carbon-coated $NiSe_2$ ($NiSe_2$@NC) electrocatalyst was prepared by successive annealing treatment. Benefiting from the synergistic effect between the $NiSe_2$ nanoparticles and NC, the $2e^-$ ORR activity, selectivity, and stability of $NiSe_2$@NC in 0.1 M $HClO_4$ was greatly enhanced, with the yield of H_2O_2 being 4.4 times that of the bare $NiSe_2$ nanoparticles. The in situ Raman spectra and density functional theory (DFT) calculation revealed that the presence of NC was beneficial for regulating the electronic state of $NiSe_2$ and optimizing the adsorption free energy of *OOH, which could enhance the adsorption of O_2, stabilize the O-O bond, and boost the production of H_2O_2. This work provides an effective strategy to improve the performance of the transition metal chalcogenide for $2e^-$ ORR to H_2O_2.

Keywords: two-electron oxygen reduction reaction; hydrogen peroxide; $NiSe_2$ nanoparticles; nitrogen-doped carbon

Citation: Cheng, Q.; Ding, H.; Chen, L.; Dong, J.; Yu, H.; Yan, S.; Wang, H. Modification of $NiSe_2$ Nanoparticles by ZIF-8-Derived NC for Boosting H_2O_2 Production from Electrochemical Oxygen Reduction in Acidic Media. *Catalysts* **2024**, *14*, 364. https://doi.org/10.3390/catal14060364

Academic Editor: Carlo Santoro

Received: 11 May 2024
Revised: 27 May 2024
Accepted: 31 May 2024
Published: 3 June 2024

1. Introduction

Hydrogen peroxide (H_2O_2) has been a high-value-added chemical with wide applications [1–3]. The industrial production of H_2O_2 uses an anthraquinone process, which has many disadvantages such as high energy consumption and pollution [4–6]. In contrast, the preparation of H_2O_2 using electrocatalytic oxygen reduction can be carried out at room temperature and pressure. The environment-friendly electrosynthesis of H_2O_2 through $2e^-$ ORR is regarded as a promising alternative [7,8]. As is generally known, ORR is an electrocatalytic reaction proceeding with a four-electron ($4e^-$) pathway or two-electron ($2e^-$) pathway when applying different electrocatalysts. The $4e^-$ ORR reaction has been intensively studied and applied in battery conversion systems such as fuel cells or metal–air batteries [9–11], while the development of efficient electrocatalysts for the selective $2e^-$ ORR pathway toward H_2O_2 remains challenging at present [1,9].

To date, various catalysts have been developed for electrocatalytic oxygen reduction to produce H_2O_2, but most of them showed a significantly improved $2e^-$ ORR performance only under alkaline media [12–15]. However, from the perspective of practical application, H_2O_2 is prone to decomposition in the alkaline environment for a long time, which greatly limits its application in actual industry and daily life [16–18]. On the contrary, acidic media can not only effectively stabilize H_2O_2, but it can also be more suitable for application scenarios such as electro-Fenton, showing more attractive advantages [7,19–21]. Therefore,

researchers tend to develop high-performance electrocatalysts under acidic media. Precious metal-based catalysts have been approved to show the best $2e^-$ ORR performance under acidic media, but are limited by their high cost and scarcity [22–24]. Therefore, transition metal chalcogenides have attracted more attention because of their advantages such as their low cost, abundant reserves, high stability, and easy adjustment of electronic structure [25–27].

In particular, transition metal selenides (TMSs) have been regarded as a promising $2e^-$ ORR catalyst under acidic media [28–30]. $NiSe_2$ is a typical TMS catalyst, but most reports focus on the field of water splitting or energy storage in previous studies [31,32]. Recently, $NiSe_2$ has also been confirmed to be effective for $2e^-$ ORR reaction [33]. Due to the large atomic radius, high electronegativity of the Se element, and metal-like property, $NiSe_2$ can effectively weaken the interactions of the outer metal electrons and then optimize the activation of oxygen-containing intermediates to promote the generation of H_2O_2. However, $NiSe_2$ often exhibits poor electrical conductivity and tends to aggregate into larger particles, which could affect the electron transfer rate [34,35]. It is well-known that the carbon materials have a high electrical conductivity and stability; in the meantime, they could stabilize the nanoparticles as the supports or coating agents [36,37]. Accordingly, compositing $NiSe_2$ with highly conductive carbon materials could make use of both advantages to facilitate the formation of H_2O_2 from $2e^-$ ORR in acidic media. In addition, metal–organic frameworks (MOFs) have the advantages of large porosity, large surface area, and tunable morphology and structure, and they are often used as an effective precursor for preparing efficient electrocatalysts [38]. Therefore, using MOFs precursors could provide a good platform for the effective combination of $NiSe_2$ with a carbon material.

Based on the above considerations, in order to enhance the $2e^-$ ORR performance of $NiSe_2$, a nitrogen-doped carbon-coated $NiSe_2$ ($NiSe_2$@NC) electrocatalyst was fabricated using ZIF-8 as the N-doped carbon precursor. The results showed that the introduction of NC could promote $NiSe_2$ to form small-particle-size nanoparticles. In comparing with the bare $NiSe_2$, $NiSe_2$@NC could achieve a significantly improved H_2O_2 Faraday efficiency of 73% to 81%, H_2O_2 yield of 12 ppm to 53 ppm in 2 h if electrolysis, and long-term stability of 10 h in an H-type cell. In situ Raman spectroscopy and DFT calculation revealed that $NiSe_2$@NC was beneficial for adjusting the electronic state of $NiSe_2$ and optimizing the adsorption free energy of *OOH, which was conducive to promoting $2e^-$ ORR to produce H_2O_2. This work hopefully provides a valuable reference for the development of more efficient transition metal electrocatalysts toward $2e^-$ ORR.

2. Results and Discussion

2.1. Material Characterizations

The synthetic procedure of $NiSe_2$@NC is displayed in Figure 1, which is prepared by the impregnation of Ni^{2+} with ZIF-8 and the successive annealing treatment, respectively. Firstly, Ni^{2+} ions were introduced into the self-assembled ZIF-8 to form Ni-ZIF-8. Then, the annealing treatment at 1000 °C under an Ar atmosphere was applied to form Ni-N-C. The subsequent pyrolysis process with selenium powder at 500 °C was performed to obtain the $NiSe_2$@NC catalyst.

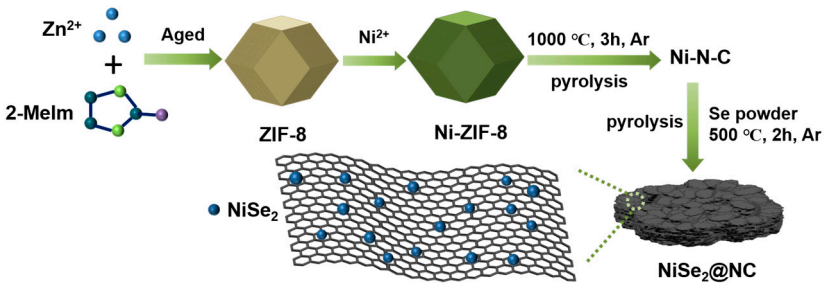

Figure 1. Schematic illustration of fabrication process of $NiSe_2$@NC catalyst.

The morphologies of the catalysts were characterized by scanning electron microscopy (SEM) and transmission electron microscopy (TEM). As shown in Figure S1a, the ZIF-8 samples exhibit a rhombic dodecahedral morphology with the diameter of 200~250 nm. Figure 2a displays the N-doped carbon (NC) samples with a pristine morphology by the annealing treatment of ZIF-8 at 1000 °C under an Ar atmosphere, which have a smaller size (100~200 nm) than ZIF-8. And there is no formation of metal nanoparticles inside (Figure 2d), implying that the Zn NPs formed by annealing are completely removed under high-temperature calcination. The as-prepared $NiSe_2$@NC samples (Figure 2b,e) show a disordered structure and a rough surface containing small nanoparticles (10~20 nm), indicating the successful composite of metal and NC. In contrast, pure $NiSe_2$ particles (Figure 2c,f) show much larger aggregated particles in the absence of carbon carriers. Furthermore, the high-resolution TEM image (HRTEM) in Figure 2g shows that the lattice fringe of the nanoparticles is 0.266 nm, which corresponds to the (210) plane of $NiSe_2$ [33], again validating the successful combination of $NiSe_2$ and NC. Moreover, the elemental mapping images of $NiSe_2$@NC shown in Figure 2h–k further indicate the presence of C, Ni, Se, and N elements and uniform distribution. These results imply that N-doped carbon-coated $NiSe_2$ catalysts were prepared successfully. Meanwhile, the $NiSe_2$ nanoparticles with a small particle size in $NiSe_2$@NC could be beneficial to expose more reactive active sites and thus obtain a higher ORR activity.

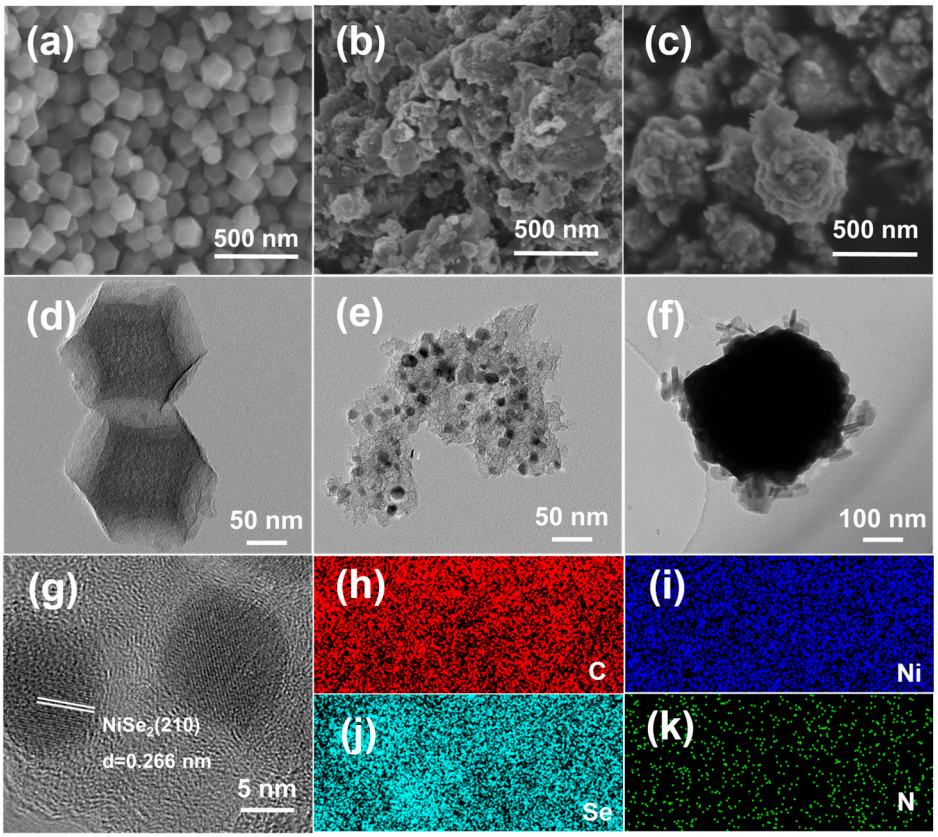

Figure 2. SEM images of (**a**) NC, (**b**) $NiSe_2$@NC, and (**c**) $NiSe_2$. TEM images of (**d**) NC, (**e**) $NiSe_2$@NC, and (**f**) $NiSe_2$. (**g**) HRTEM image of $NiSe_2$@NC. (**h**–**k**) The SEM elemental mapping of $NiSe_2$@NC.

The composition and the crystal structure of the samples were characterized by X-ray diffraction (XRD). The characteristic diffraction peaks of ZIF-8 (Figure S1b) are consistent with previous reports [39]. As shown in Figure 3a, NC has wide diffraction peaks at 24.8° and 43.6°, which can be indexed to the (002) and (100) planes of carbon, respectively. Both $NiSe_2$@NC and $NiSe_2$ show peaks at 29.8°, 33.5°, 36.8°, 42.8°, 50.6°, 55.4°, 57.8°, 62.2°, and 72.6°, corresponding to the (200), (210), (211), (220), (311), (230), (321), (400), and (421)

planes of $NiSe_2$ (PDF#65-1843) [40], respectively, which further confirms the successful synthesis of the $NiSe_2$@NC catalyst. Combined with the Scherrer equation, the average crystal size of $NiSe_2$ nanoparticles in $NiSe_2$@NC could be calculated to be 20.2 nm, which is consistent with the TEM characterization result. In addition, the carbon properties were characterized by Raman spectroscopy as shown in Figure 3b. Both NC and $NiSe_2$@NC have two characteristic peaks at 1350 cm^{-1} and 1590 cm^{-1}, corresponding to the D and G bands of carbon, respectively. The D band represents disordered or defective carbon and the G band represents graphitized carbon [41]. The I_D/I_G values of NC and $NiSe_2$@NC are 0.86 and 0.90, respectively, indicating the presence of defects in both catalysts, which have been reported to favor ORR activity [42].

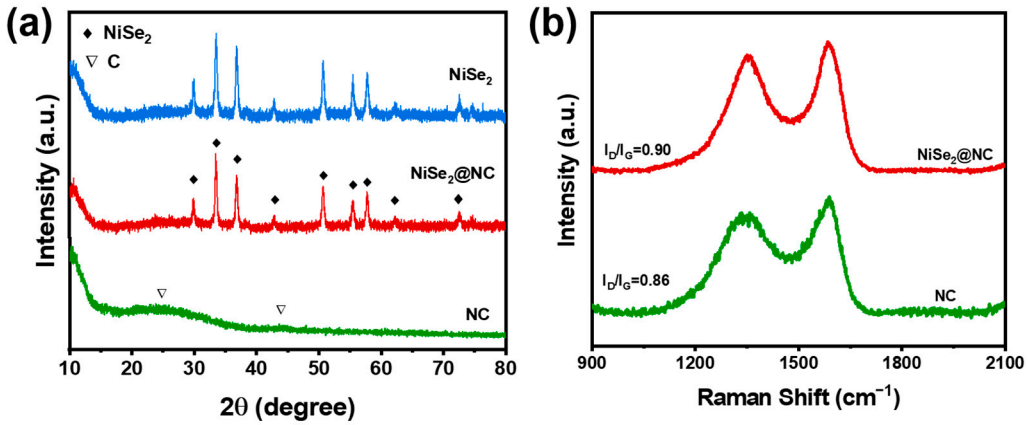

Figure 3. (**a**) XRD patterns and (**b**) Raman spectra of NC, $NiSe_2$@NC, and $NiSe_2$.

For comparison, the other two $NiSe_2$@NC samples ($NiSe_2$@NC-L and $NiSe_2$@NC-H) with lower and higher Ni addition were prepared under the same condition, respectively. Their morphologies and compositions were also observed. As shown in Figure S2a,b, the morphology of $NiSe_2$@NC-H is similar to that of $NiSe_2$@NC, while a large number of tubular structures exist in $NiSe_2$@NC-L. The XRD pattern of $NiSe_2$@NC-L (Figure S2c) shows a series of characteristic diffraction peaks of $NiSe_2$ (PDF#65-1843) and a sharp diffraction peak at 26°, which is attributed to the (002) plane of graphitized carbon, corresponding to the formed carbon nanotubes [43]. In the case of increasing the Ni^{2+} addition, the diffraction peaks of $NiSe_2$ disappear in $NiSe_2$@NC-H, and new characteristic peaks appear at 33.0°, 44.6°, 50.5°, 60.2°, 61.6°, and 69.6°, which can be well indexed to $Ni_{0.85}Se$ (PDF#18-0888) [44]. These results indicate that the amount of Ni precursor addition could affect the formation of nickel selenide, and the $NiSe_2$ phase could gradually transform into the $Ni_{0.85}Se$ phase with the increase in Ni addition.

The composition and valence state of $NiSe_2$@NC were further determined by X-ray photoelectron spectroscopy (XPS). The signal peaks of C 1s, N 1s, Ni 2p, and Se 3d can be observed in Figure S3, confirming the existence of the four elements. The C 1s spectrum (Figure 4a) can be divided into two peaks ascribed to C-C (284.8 eV) and C-N (285.7 eV) [45]. The N 1s spectrum can be divided into three peaks at 398.2 eV, 400.0 eV, and 401.8 eV, corresponding to pyridinic N, pyrrolic N, and graphitic N, respectively (Figure 4b) [46]. The Ni 2p spectrum in Figure 4c shows the peak signals of Ni $2p_{3/2}$ and Ni $2p_{1/2}$. The fitting peaks at the binding energy of 853.4 eV and 870.9 eV are related to Ni^{2+}, and the peaks at 855.6 eV and 873.8 eV are ascribed to Ni^{3+} (oxidation state). And the other two peaks at 860.1 eV and 879.1 eV can be assigned to the satellite peaks [47]. The Se 3d spectrum in Figure 4d has two peaks at 54.8 eV and 55.6 eV, which correspond to Se $3d_{5/2}$ and Se $3d_{3/2}$, indicating the existence form of Se_2^{2-} [48]. And the peak at 59.0 eV can be assigned to oxidized Se (SeO_x) [37,48].

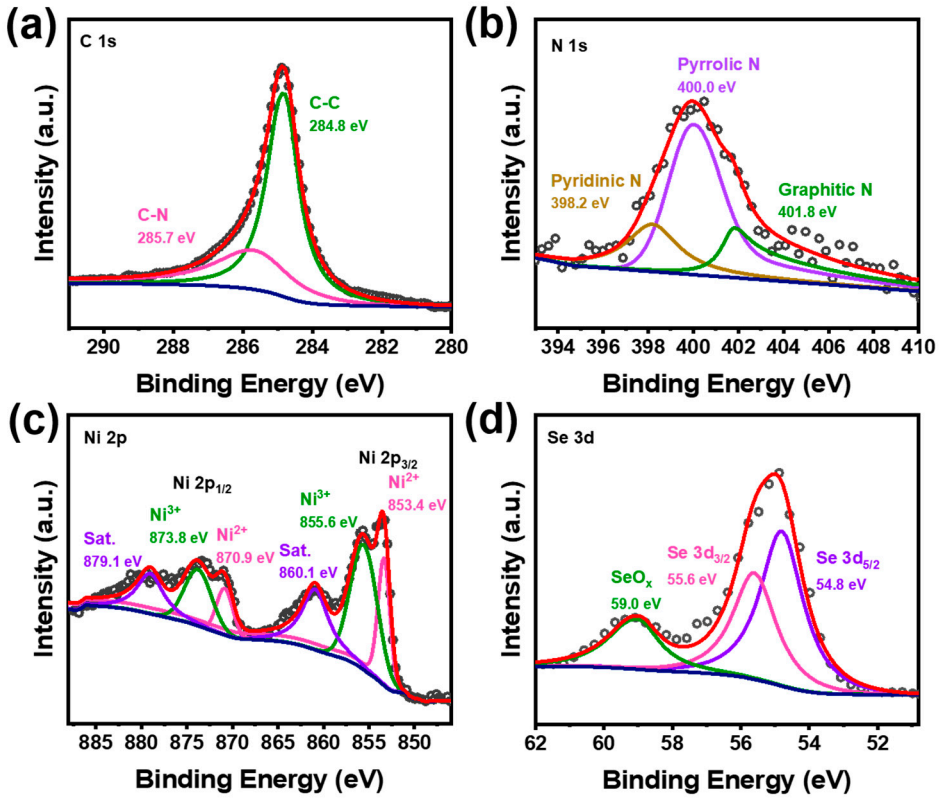

Figure 4. (**a**) C 1s diagram, (**b**) N 1s diagram, (**c**) Ni 2p diagram, and (**d**) Se 3d diagram of $NiSe_2$@NC, where the circles represent the raw data and the red lines represent the fitted data.

2.2. Electrocatalytic Performance

The $2e^-$ ORR performance of NC, $NiSe_2$@NC, and $NiSe_2$ were evaluated by the RRDE system in O_2-saturated 0.1 M $HClO_4$. According to the polarization curves shown in Figure 5a, NC has the most positive onset potential (0.57 V vs. RHE), followed by $NiSe_2$@NC (0.55 V vs. RHE) and $NiSe_2$ (0.54 V vs. RHE). The disk current densities also present the same changing trend, which means NC has the highest ORR reaction kinetics among the three catalysts. Obviously, $NiSe_2$@NC also shows a better ORR activity than bare $NiSe_2$ due to the combination with N-doped carbon. Figure 5b shows the ring current densities of the three catalysts at different potentials. Compared with the other two catalysts, $NiSe_2$@NC has the highest ring current density, which is about 1.2 and 1.8 times that of NC and $NiSe_2$ at 0 V vs. RHE, respectively. This trend means that more O_2 is converted to H_2O_2, which can be confirmed by the H_2O_2 selectivity and electron transfer number in Figure 5c,d. $NiSe_2$@NC has the highest H_2O_2 selectivity of 77% and the lowest electron transfer number at 0.3 V vs. RHE. The selectivity of H_2O_2 of $NiSe_2$ is 68% at the same potential. It can also be seen that the selectivity of NC is the lowest, only 38~59%. These results indicate that the combination of $NiSe_2$ and NC is more beneficial to the $2e^-$ pathway than that of the pure component. Among the catalysts with different degrees of selenization, $NiSe_2$@NC-H shows the lowest ORR activity (Figure S4), which may be related to the existence form of $Ni_{0.85}Se$ that is not conducive to the reaction under acidic media. Moreover, $NiSe_2$@NC also exhibits the best $2e^-$ ORR activity and selectivity.

In addition, the ORR performance of $NiSe_2$@NC under alkaline media (0.1 M KOH) was also evaluated, as shown in Figure S5. $NiSe_2$@NC exhibits an excellent ORR activity with an initial potential of 0.79 V vs. RHE and a disk current density of 2.8 mA cm^{-2} at 0 V vs. RHE. However, the ring current density is drastically reduced with only ~35% H_2O_2 selectivity, which is much lower than the performance tested under acidic media. The results suggest that $NiSe_2$@NC is more favorable for electrocatalytic oxygen reduction for H_2O_2 production under acidic media.

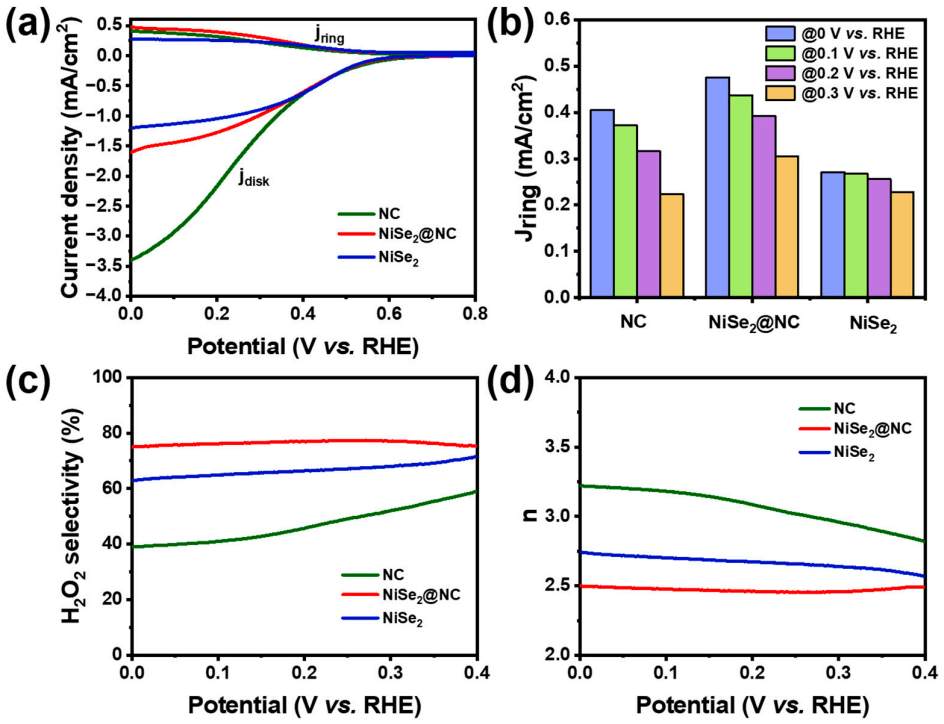

Figure 5. (**a**) RRDE polarization curves, (**b**) ring current densities at different potentials, (**c**) H_2O_2 selectivity, and (**d**) electron transfer number of NC, $NiSe_2$@NC, and $NiSe_2$ at 1600 rpm in O_2-saturated 0.1 M $HClO_4$.

To reveal the effect of the combination of $NiSe_2$ and NC on the improved catalytic performance, other electrochemical properties were further tested. Figure 6a shows the Nyquist plots and fitted charge transfer resistance of the three catalysts to reveal the electronic conductivity [49,50]. The metal-free NC has the smallest semicircular diameter, corresponding to the highest disk current in the LSV curves. In addition, compared with the bare $NiSe_2$, $NiSe_2$@NC also exhibits a smaller semicircular diameter and lower charge transfer resistance, implying a higher electronic conductivity than $NiSe_2$. The cyclic voltammetry curves of the double-layer region (Figure S6) were also performed at different scan rates, which could be used to measure the electrochemical active surface area (ECSA). As seen in Figure 6b, the double-layer capacitance (C_{dl}) of NC is 2.9 mF cm^{-2}. It is followed by $NiSe_2$@NC with the C_{dl} value of 0.86 mF cm^{-2}, which is 2.7 times higher than that of $NiSe_2$ (0.32 mF cm^{-2}), revealing a higher active surface area [15]. These results indicate that the combination with NC can not only improve the conductivity of $NiSe_2$, but also expose more active sites.

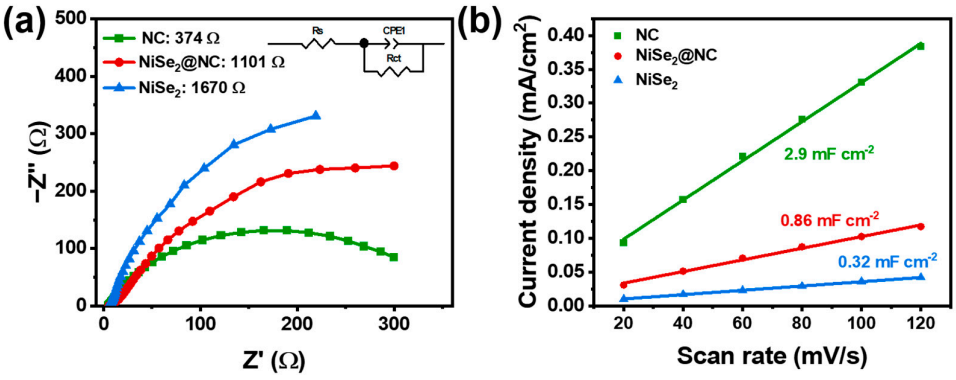

Figure 6. (**a**) Nyquist plots and (**b**) double-layer capacitance measured for NC, $NiSe_2$@NC, and $NiSe_2$.

The Faraday efficiency (FE) and yield of H_2O_2 are also important indicators to evaluate the practical application of catalysts [51]. Therefore, the actual H_2O_2 production capacity of $NiSe_2$@NC was evaluated by electrolysis of 7200 s in an H-type cell, combined with UV–Vis spectra of Ce^{4+} at 319 nm. The electrolytic tests were performed at different potentials to determine the optimal potential of $NiSe_2$@NC. According to Figure S7a,b, the chronoamperometry curves show significantly increased current densities with the negative shift of potential. And the absorbance of Ce^{4+} also decreases correspondingly, indicating that more H_2O_2 is produced. This could be confirmed from the calculated Faraday efficiency (FE) and H_2O_2 concentration of $NiSe_2$@NC in Figure 7a. The highest Faraday efficiency of 81% can be achieved at 0.3 V vs. RHE. Meanwhile, the H_2O_2 concentration increases continuously as the potential becomes negative, with the maximum of 68 ppm at 0.2 V vs. RHE. In general, $NiSe_2$@NC has the best catalytic performance at 0.3 V vs. RHE. Subsequently, the electrochemical performance of H_2O_2 production from NC, $NiSe_2$@NC, and $NiSe_2$ was compared at 0.3 V vs. RHE, as shown in Figure 7b. Note that the $NiSe_2$@NC has a higher Faraday efficiency (81%) and H_2O_2 concentration (53 ppm) than that of NC (59%, 38 ppm) and $NiSe_2$ (73%, 12 ppm), which is consistent with the RRDE trend. It can be seen that $NiSe_2$@NC has the best H_2O_2 production capacity, which also proves that the combination of $NiSe_2$ and NC plays a great role in enhancing the performance of $2e^-$ ORR.

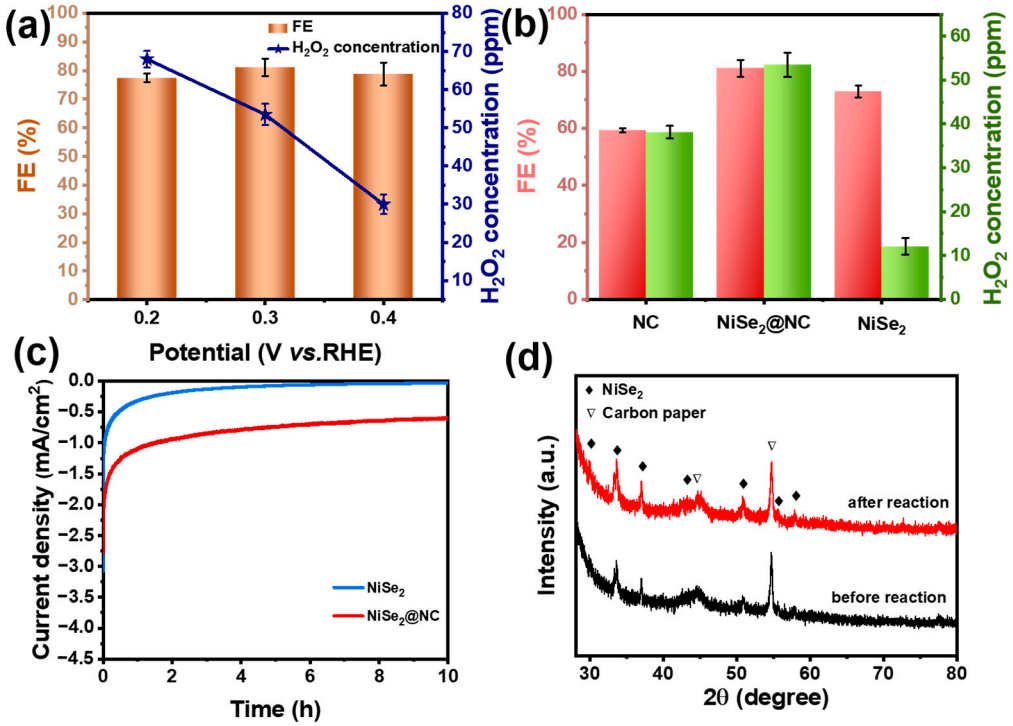

Figure 7. (**a**) Faraday efficiency and H_2O_2 concentration of $NiSe_2$@NC at different potentials for 7200 s in O_2-saturated 0.1 M $HClO_4$. (**b**) Faraday efficiency and H_2O_2 concentration of NC, $NiSe_2$@NC, $NiSe_2$ at 0.3 V vs. RHE. (**c**) Long-term stability of $NiSe_2$@NC and $NiSe_2$ at 0.4 V vs. RHE for 10 h. (**d**) XRD patterns of $NiSe_2$@NC before and after electrolysis.

The stability is another important factor to evaluate the performance of catalysts in practical applications. Therefore, the 10 h electrolysis experiments were performed at 0.4 V vs. RHE to evaluate the stability of $NiSe_2$@NC and $NiSe_2$ (Figure 7c). Obviously, the chronoamperometry curve of bare $NiSe_2$ exhibits a much higher loss in current density than $NiSe_2$@NC. According to the XRD patterns in Figure 7d and the wide range of patterns in Figure S8, the crystal structure of $NiSe_2$@NC could not be destroyed after the long-term electrolysis. Combined with the above analysis results, the introduction of NC can significantly improve the stability of the catalytic system in 0.1 M $HClO_4$, which is more

conducive to the production of H_2O_2. Table S1 compares the $2e^-$ ORR performance of other reported transition metal chalcogenides. It can be seen that $NiSe_2$@NC is a promising $2e^-$ ORR electrocatalyst with a high selectivity and H_2O_2 production capacity under acidic media.

2.3. Electrocatalytic Mechanism on $NiSe_2$@NC

To further investigate the catalytic mechanism of $NiSe_2$@NC during the ORR process, in situ Raman measurement was used to detect the intermediates produced during the reaction in O_2-saturated 0.1 M $HClO_4$. The Raman spectra of different potentials were collected at a 638 nm excitation wavelength. As shown in Figure 8a, the signal peak at 933 cm^{-1} can be associated to the symmetric stretching mode of ClO_4^- [52]. Another peak at 463 cm^{-1} also presents at all potentials, which may be related to the adsorption of oxygen-containing species on the surface of the catalyst, resulting in the formation of a Ni-O bond [53]. Furthermore, only the peaks of the ClO_4^- and Ni-O bond could be identified at the open circuit potential (OCP). The new peak signal located at 733 cm^{-1} appears when the potential is shifted negatively to 0.4 V vs. RHE, which is assigned to the vibration of the key intermediate *OOH [54]. And this peak intensity increases with the negative shift of potential, implying the accumulation of *OOH. These results indicate that $NiSe_2$@NC is an effective $2e^-$ ORR catalyst that can stabilize *OOH on the surface without further O-O bond breaking.

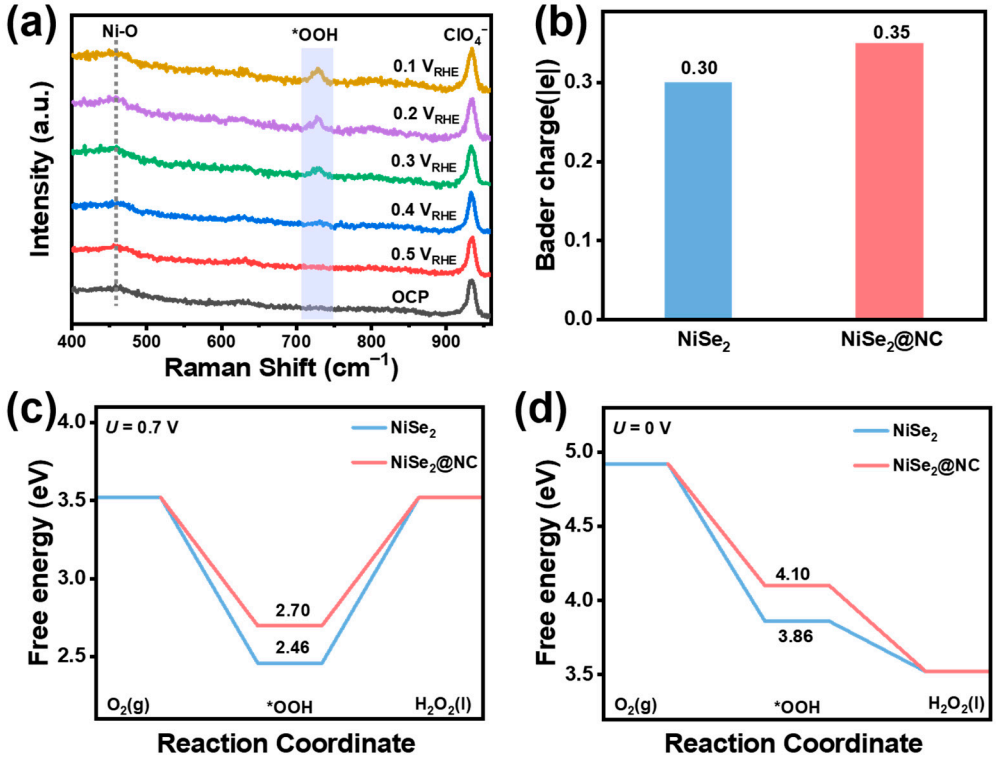

Figure 8. (**a**) In situ Raman spectra of $NiSe_2$@NC in O_2-saturated 0.1 M $HClO_4$, where the * in *OOH represents the active site of the reaction. (**b**) Bader charges of $NiSe_2$ and $NiSe_2$@NC. Free energy diagram for $2e^-$ ORR on $NiSe_2$ and $NiSe_2$@NC at (**c**) U = 0.7 V and (**d**) U = 0 V.

Based on the above in situ Raman results, density functional theoretical (DFT) calculations were carried out to further illustrate how the introduction of NC enhanced the $2e^-$ ORR activity and selectivity. The optimized simulation models of *OOH absorbed on $NiSe_2$ and $NiSe_2$@NC are exhibited in Figures S9 and S10. Undoubtedly, the pathway of the oxygen reduction reaction is mainly determined by the *OOH adsorption strength on the surface of the catalyst, which is also closely related to the electronic state of the active site [33]. Therefore, Bader charge analysis was performed to reveal the different

electronic states of $NiSe_2$ and $NiSe_2$@NC. As shown in Figure 8b, the active sites of $NiSe_2$ and $NiSe_2$@NC obtain 0.30 e and 0.35 e, respectively. Therefore, the active site of $NiSe_2$@NC has more electrons and carries more negative charge than $NiSe_2$, which is conducive to the adsorption of O_2 and H^+ during the $2e^-$ ORR reaction pathway. These results verify that the introduction of NC could effectively promote the adsorption and activation of oxygen on the active site to further produce *OOH intermediates.

The ideal $2e^-$ ORR reaction requires an optimum balance between the adsorption and desorption of *OOH, with neither too strong nor too weak an adsorption strength. Then, the *OOH adsorption free energies (ΔG_{*OOH}) of the two catalysts were calculated at the equilibrium potential (U = 0.7 V) and standard condition (U = 0 V) to evaluate the adsorption strength of *OOH. As shown in Figure 8c,d, the *OOH adsorption energies of $NiSe_2$@NC at U = 0.7 V and 0 V are 2.70 eV and 4.10 eV, respectively, both of which are closer to the ideal values (3.52 eV and 4.22 eV) than $NiSe_2$ (2.46 eV and 3.86 eV) [55,56]. From the above analysis, the conversion from *OOH to H_2O_2 production on the surface of the $NiSe_2$@NC catalyst is more favorable than for $NiSe_2$. In addition, the differential charge density distributions between adsorbed *OOH and substrates were also simulated and are displayed in Figure S11. In comparing the two catalysts, the adsorption site of $NiSe_2$ has more positive charges than that of $NiSe_2$@NC, indicating that $NiSe_2$ exhibits stronger charge interactions with *OOH, which may contribute to the breaking of the O-O bond. On the contrary, the *OOH adsorption on $NiSe_2$@NC is moderate, which is conducive to preserving the O-O bond and promoting the next hydrogenation to H_2O_2.

In conclusion, the above DFT results indicate that the introduction of NC could not only change the electronic state of $NiSe_2$ to promote the adsorption and activation of oxygen, but also optimize the adsorption free energy of *OOH to preserve the O-O bond and convert it to H_2O_2 during the oxygen reduction reaction. Therefore, $NiSe_2$@NC shows a significantly increased $2e^-$ ORR activity and selectivity.

3. Materials and Methods

3.1. Reagent and Chemicals

All reagents were of analytical grade and used without further purification. Zinc nitrate hexahydrate ($Zn(NO_3)_2{\cdot}6H_2O$), nickel chloride hexahydrate ($NiCl_2{\cdot}6H_2O$), and potassium hydroxide (KOH) were purchased from Aladdin Bio-technology Co., Ltd., Shanghai, China. Selenium powder (Se), methanol (CH_3OH), and anhydrous ethanol (C_2H_5OH) were obtained from Yuanli Chemical Co., Ltd., Tianjin, China. The compound 2-methylimidazole (2-melm) was purchased from Bailingwei Technology Co., Ltd., Beijing, China. The Nafion solution was purchased from Yingke United Co., Ltd., Tianjin, China.

3.2. Material Synthesis

3.2.1. Synthesis of ZIF-8

The compound ZIF-8 was synthesized based on a previous reported method with a slight adjustment [39]. Typically, 1.487 g of $Zn(NO_3)_2{\cdot}6H_2O$ and 1.644 g of 2-methylimidazole were dissolved in 50 mL of methanol solution, respectively. After mixing the two solutions, the mixture was stirred rapidly for 30 min and left at room temperature for 24 h. Finally, the white product was centrifuged, washed with ethanol, and fully dried in a vacuum drying oven at 60 °C.

3.2.2. Synthesis of $NiSe_2$@NC

A total of 200 mg of ZIF-8 was ultrasonically dispersed in 60 mL of ethanol. Then, 100 mg of $NiCl_2{\cdot}6H_2O$ was added to the above solution and stirred at room temperature for 12 h. The precipitate was centrifuged and dried to obtain Ni-ZIF-8. Subsequently, the Ni-ZIF-8 was transferred to a tube furnace and annealed at 1000 °C for 3 h with a heating rate of 5 °C min^{-1} under an Ar atmosphere to form Ni-N-C. Finally, a 2:1 mass ratio of Se powder and Ni-N-C were loaded into two porcelain boats. One of the porcelain boats containing Se powder was placed upstream of the tube furnace and annealed at 500 °C for

2 h with a heating rate of 2 °C min^{-1} under an Ar atmosphere. The samples after pyrolysis were recorded as $NiSe_2$@NC. In addition, the content of $NiCl_2 \cdot 6H_2O$ was varied during catalyst preparation by adding 50 mg and 150 mg of $NiCl_2 \cdot 6H_2O$, respectively. Other steps were carried out under the same conditions. The final samples were respectively labeled as $NiSe_2$@NC-L and $NiSe_2$@NC-H, respectively.

3.2.3. Synthesis of NC and $NiSe_2$

The NC catalyst was obtained by the direct calcination of ZIF-8 under the same conditions. The $NiSe_2$ catalyst was synthesized by a one-step hydrothermal reaction. In total, 0.24 g of $NiCl_2 \cdot 6H_2O$, 0.18 g of Se powder, and 3 g of KOH were added to 20 mL of deionized water and stirred for 30 min at room temperature. Subsequently, the mixture was transferred to an oven for 12 h at 150 °C. After the solution was cooled to room temperature, it was washed with deionized water and finally dried in a vacuum drying oven at 60 °C. The resulting samples were denoted as $NiSe_2$.

3.3. Materials Characterization

The morphology and structure of the catalyst were measured by scanning electron microscopy (SEM, S-4800, Hitachi, Tokyo, Japan) and transmission electron microscopy (TEM, JEM-2100F, Japan Electronics, Islamabad, Pakistan). The distribution of elements was determined by energy dispersive X-ray spectroscopy (EDX) using scanning electron microscopy. The crystal structure was measured using X-ray diffraction (XRD, D8 Focus, Bruck, Billerica, MA, USA) using a Cu-Kα radiation source at a scan rate of 5 °C min^{-1}. X-ray photoelectron spectroscopy (XPS, K-Alpha+, Thermo, Waltham, MA, USA) was performed to determine the composition and chemical state. Raman spectra (Horiba, Kyoto, Japan) were measured at 638 nm to determine the phase composition. The optical properties were detected by an ultraviolet–visible spectrophotometer (UV–Vis, T2600, Yoke, Shanghai, China). The crystallites' size from the XRD pattern could be calculated by the Scherrer equation.

3.4. Electrochemical Measurements

All electrochemical tests in this paper were performed using a CHI 760E electrochemical workstation (Chenhua Instrument Co., Ltd., Shanghai, China) and 0.1 M $HClO_4$. The $2e^-$ ORR performance of catalysts was evaluated using a rotating ring disk electrode (RRDE, disk area: 0.247 cm^2, platinum ring area: 0.186 cm^2) as the working electrode. Carbon rods were used as the counter electrodes and saturated calomel electrodes (SCE) as the reference electrodes to form the test system. The ink was prepared by mixing 2.5 mg of catalyst, 500 μL of ethanol, 500 μL of H_2O, and 20 μL of Nafion solution. After ultrasonic dispersion, 10 μL of ink was added to the RRDE surface with the catalyst loading of 0.1 mg cm^{-2}. Before the catalytic performance measurement, cyclic voltammetry (CV) was performed on catalyst-loaded RRDE under a N_2 atmosphere, scanning in the potential range from 0 to 0.8 V vs. a reversible hydrogen electrode (RHE) at 50 mV s^{-1} for around 20 cycles. After the CV curves remained stable, the linear voltametric sweep (LSV) test was performed in O_2-saturated 0.1 M $HClO_4$. In the same potential range, LSV curves were measured at a scan rate of 5 mV s^{-1} and a rotating speed of 1600 rpm. Moreover, the Pt ring voltage was kept at 1.3 V vs. RHE during the test. The selectivity of H_2O_2 and electron transfer number (n) were calculated according to the following formula:

$$H_2O_2(\%) = 200 \times I_r / [(N \times I_d) + I_r] \quad (1)$$

$$n = 4 \times I_d / (I_d + I_r / N) \quad (2)$$

where I_d is the disk current, I_r is the ring current, and N is the collection efficiency of the Pt ring, which could be identified by the LSV curves at different speeds. As shown in Figure S12, the collection efficiency is 37%.

The Faraday efficiency (FE) and yield of H_2O_2 are determined by the chromogenic reaction of $Ce(SO_4)_2$ ($2Ce^{4+} + H_2O_2 \rightarrow 2Ce^{3+} + 2H^+ + O_2$). In the presence of H_2O_2, $Ce(SO_4)_2$ (yellow) can be converted to Ce^{3+} (colorless), which could reduce the absorbance of UV–Vis at 319 nm. Therefore, the H_2O_2 production capacity of the catalyst can be measured by the change in absorbance. The standard solution of $Ce(SO_4)_2$ with different concentrations was configured by dissolving $Ce(SO_4)_2$ in a 0.5 M H_2SO_4 solution. According to the UV–Vis peak absorbance and Ce^{4+} concentration, the standard curve is drawn in Figure S13 (y = 4.084x − 0.0312). The electrolytic process is carried out in an H-type cell, as shown in Figure S14. A 1 × 1 cm^2 carbon paper supported with the catalyst was used as the working electrode, saturated calomel electrodes as the reference electrodes, and the Pt sheet as the counter electrode. After two hours of electrolysis, 50 μL of electrolytic solution was added to 3 mL of 0.5 mM $Ce(SO_4)_2$ solution, and then the change in the peak absorbance of Ce^{4+} was recorded. The FE and yield of H_2O_2 can be calculated according to the following formula:

$$FE(\%) = 200 \times C \times V \times F/Q \quad (3)$$

$$[H_2O_2]\ (ppm) = \frac{1}{2} \times \frac{V_1 \times C_{before} - (V_1 + V_2) \times C_{after}}{V_2} \times 34.01 \quad (4)$$

where C is the concentration of the H_2O_2 product (mol L^{-1}), V is the volume of the solution in the electrolytic cell (L), F is the Faraday constant (96,485 C mol^{-1}), V_1 is the volume of Ce^{4+} before the reaction (mL), C_{before} is the concentration of Ce^{4+} before the reaction (mmol L^{-1}), V_2 is the volume of the added electrolyte solution (mL), and C_{after} is the concentration of Ce^{4+} after the reaction (mmol L^{-1}).

And in this work, all of the measured SCE potentials were converted to the reversible hydrogen electrode (RHE) potentials according to the following formula:

$$E_{RHE} = E_{SCE} + 0.059\ pH + 0.233 \quad (5)$$

3.5. Computational Method

All calculations in this work were performed using the VASP software package (5.4.4). The GGA-PBE function is used to describe the exchange correlation interaction, the PAW method is used to describe the direct interaction between nuclei and valence electrons, and the DFT-D3 method is used to modify the van der Waals interaction. The convergence criteria for energy and force are 10^{-4} eV and 0.05 eV/Å. The plane wave truncation energy is set to 400 eV, and a 3 × 3 × 1 K-point grid is used to optimize the geometric structure and calculate the frequency and electronic characteristics of the catalyst. The optimal $NiSe_2$ exposed crystal surface is (210), the catalyst is set to a thickness of 3 layers, and the $NiSe_2$ is p (2 × 1) period units. The graphene carrier is a 4 × 3 supercell containing 48 carbon atoms, and a 15 Å vacuum layer is added to reduce the interaction between adjacent layers. The free energy is calculated according to the following formula:

$$G = E_{elect} + E_{ZPE} - TS + G_U \quad (6)$$

where E_{elect} is the electronic energy calculated by DFT, E_{ZPE} and S are the zero-point energy and entropy, T is 298.15 K, and $G_U = -n_eU$.

4. Conclusions

In summary, we present a nitrogen-doped carbon-coated $NiSe_2$ ($NiSe_2$@NC) electrocatalyst for boosting the H_2O_2 production from $2e^-$ ORR in acidic media. $NiSe_2$@NC exhibited the better $2e^-$ ORR activity and selectivity, with the yield of H_2O_2 being 4.4 times that of bare $NiSe_2$. In addition, the long-term stability of 10 h could be achieved in the electrolysis process. This significantly improved $2e^-$ ORR performance was mainly attributed to the synergistic effect of $NiSe_2$ and NC. The introduction of NC could reduce the charge transfer resistance and stabilize the $NiSe_2$ nanoparticles to expose a greater electrochemically active surface area. Moreover, in situ Raman tests and DFT calculations were further performed

to reveal the role of the composition of $NiSe_2$ with NC. The introduction of NC could not only adjust the electronic state of $NiSe_2$ to carry more negative charges on the active site, but it could also optimize the adsorption free energy of *OOH, thus further promoting $2e^-$ ORR for the production of H_2O_2. This work provides an effective strategy to modify the transition metal selenides for selectively producing H_2O_2 by the $2e^-$ ORR reaction under acidic media.

Supplementary Materials: The following supporting information can be downloaded at https://www.mdpi.com/article/10.3390/catal14060364/s1. Figure S1: (a) SEM image and (b) XRD pattern of ZIF-8; Figure S2: SEM images of (a) $NiSe_2$@NC-L and (b) $NiSe_2$@NC-H. (c) XRD patterns of $NiSe_2$@NC-L and $NiSe_2$@NC-H; Figure S3. XPS full spectrum of $NiSe_2$@NC; Figure S4: (a) RRDE polarization curves, (b) H_2O_2 selectivity and electron transfer number of $NiSe_2$@NC-L, $NiSe_2$@NC, and $NiSe_2$@NC-H at 1600 rpm in O_2-saturated 0.1 M $HClO_4$; Figure S5: (a) RRDE polarization curves and (b) H_2O_2 selectivity of $NiSe_2$@NC at 1600 rpm in O_2-saturated 0.1 M KOH; Figure S6: Cyclic voltammograms of (a) NC, (b) $NiSe_2$@NC, and (c) $NiSe_2$ at different scan rates; Figure S7: (a) Chronoamperometry curves for $NiSe_2$@NC at different potentials for 7200 s in O_2-saturated 0.1 M $HClO_4$ and (b) the corresponding UV–Vis spectra; Figure S8: XRD patterns of $NiSe_2$@NC before and after electrolysis over a wide range; Figure S9: The DFT calculation models of $NiSe_2$-OOH, where the yellow, blue, red, and white spheres represent the Se, Ni, O, and H atoms, respectively; Figure S10: The DFT calculation models of $NiSe_2$@NC-OOH, where the yellow, blue, red, white, and gray spheres represent the Se, Ni, O, H, and C atoms, respectively; Figure S11: Differential charge density distributions between adsorbed *OOH and (a) $NiSe_2$ and (b) $NiSe_2$@NC substrates, where the green, gray, and brown spheres represent the Se and Ni atom, respectively, while the cyan and yellow color isosurfaces mean the negative and positive charge, respectively; Figure S12: (a) LSV curves of RRDE at different speeds and (b) linear fitting curve of the disk current and ring current; Figure S13: (a) UV–Vis spectra of different standard Ce^{4+} solution and (b) the corresponding standard curve. Figure S14: Diagram of an H-type electrolytic cell reaction device; Table S1: Comparison of $2e^-$ ORR properties with other transition metal chalcogenides. References [26,27,33,36,37,57–60] are cited in the Supplementary Materials.

Author Contributions: Conceptualization, Q.C. and H.W.; data curation, Q.C., H.D., L.C., J.D., H.Y., S.Y. and H.W.; formal analysis, Q.C. and H.D.; funding acquisition, H.W.; investigation, Q.C.; methodology, Q.C. and H.D.; project administration, H.W.; resources, H.W.; supervision, H.W.; validation, H.W.; visualization, Q.C.; writing—original draft, Q.C.; writing—review and editing, H.W. All authors have read and agreed to the published version of the manuscript.

Funding: This research was funded by the National Natural Science Foundation of China (Grant No. 22178266).

Data Availability Statement: Data are available within the article.

Acknowledgments: We are grateful to the analysis and test center of Tianjin University for providing XRD, SEM, and XPS characterizations. We are also grateful to the Donghai Mei group in Tiangong University for providing in situ Raman spectroscopy tests.

Conflicts of Interest: The authors declare no conflicts of interest.

References

1. Tian, Y.; Deng, D.; Xu, L.; Li, M.; Chen, H.; Wu, Z.; Zhang, S. Strategies for Sustainable Production of Hydrogen Peroxide via Oxygen Reduction Reaction: From Catalyst Design to Device Setup. *Nano-Micro Lett.* **2023**, *15*, 122. [CrossRef] [PubMed]
2. Peng, W.; Tan, H.; Liu, X.; Hou, F.; Liang, J. Perspectives on Carbon-Based Catalysts for the Two-Electron Oxygen Reduction Reaction for Electrochemical Synthesis of Hydrogen Peroxide: A Minireview. *Energy Fuels* **2023**, *37*, 17863–17874. [CrossRef]
3. Jung, E.; Shin, H.; Hooch Antink, W.; Sung, Y.-E.; Hyeon, T. Recent Advances in Electrochemical Oxygen Reduction to H_2O_2: Catalyst and Cell Design. *ACS Energy Lett.* **2020**, *5*, 1881–1892. [CrossRef]
4. Wang, N.; Ma, S.; Zuo, P.; Duan, J.; Hou, B. Recent Progress of Electrochemical Production of Hydrogen Peroxide by Two-Electron Oxygen Reduction Reaction. *Adv. Sci.* **2021**, *8*, 2100076. [CrossRef] [PubMed]
5. Wu, Y.; Sun, J.; Dou, S.; Sun, J. Non-precious metal electrocatalysts for two-electron oxygen electrochemistry: Mechanisms, progress, and outlooks. *J. Energy Chem.* **2022**, *69*, 54–69. [CrossRef]
6. Ali, I.; Van Eyck, K.; De Laet, S.; Dewil, R. Recent advances in carbonaceous catalyst design for the in situ production of H_2O_2 via two-electron oxygen reduction. *Chemosphere* **2022**, *308*, 136127. [CrossRef] [PubMed]

7. Zhang, Q.; Zheng, L.; Gu, F.; Wu, J.; Gao, J.; Zhang, Y.-C.; Zhu, X.-D. Recent advances in single-atom catalysts for acidic electrochemical oxygen reduction to hydrogen peroxide. *Nano Energy* **2023**, *116*, 108798. [CrossRef]
8. Liu, K.; Li, F.; Zhan, H.; Zhan, S. Recent progress in two-dimensional materials for generation of hydrogen peroxide by two-electron oxygen reduction reaction. *Mater. Today Energy* **2024**, *40*, 101500. [CrossRef]
9. Du, M.; Li, D.; Liu, S.; Yan, J. Practical Classification of Catalysts for Oxygen Reduction Reactions: Optimization Strategies and Mechanistic Analysis. *Adv. Funct. Mater.* **2023**, *33*, 2301527. [CrossRef]
10. Bhuvanendran, N.; Ravichandran, S.; Xu, Q.; Maiyalagan, T.; Su, H. A quick guide to the assessment of key electrochemical performance indicators for the oxygen reduction reaction: A comprehensive review. *Int. J. Hydrog. Energy* **2022**, *47*, 7113–7138. [CrossRef]
11. Xu, X.; Pan, Y.; Zhong, Y.; Ran, R.; Shao, Z. Ruddlesden–Popper perovskites in electrocatalysis. *Mater. Horiz.* **2020**, *7*, 2519–2565. [CrossRef]
12. Wang, Z.; Li, Q.-K.; Zhang, C.; Cheng, Z.; Chen, W.; McHugh, E.A.; Carter, R.A.; Yakobson, B.I.; Tour, J.M. Hydrogen Peroxide Generation with 100% Faradaic Efficiency on Metal-Free Carbon Black. *ACS Catal.* **2021**, *11*, 2454–2459. [CrossRef]
13. Liu, M.; Su, H.; Cheng, W.; Yu, F.; Li, Y.; Zhou, W.; Zhang, H.; Sun, X.; Zhang, X.; Wei, S.; et al. Synergetic Dual-Ion Centers Boosting Metal Organic Framework Alloy Catalysts toward Efficient Two Electron Oxygen Reduction. *Small* **2022**, *18*, 2202248. [CrossRef] [PubMed]
14. Fu, H.; Zhang, N.; Lai, F.; Zhang, L.; Wu, Z.; Li, H.; Zhu, H.; Liu, T. Lattice Strained B-Doped Ni Nanoparticles for Efficient Electrochemical H_2O_2 Synthesis. *Small* **2022**, *18*, 2203510. [CrossRef] [PubMed]
15. Zhang, Y.; Chen, Q.; Guo, A.; Wang, X.; Wang, Y.; Long, Y.; Fan, G. Carbon-nanosheet-driven spontaneous deposition of Au nanoparticles for efficient electrochemical utilizations toward H_2O_2 generation and detection. *Chem. Eng. J.* **2022**, *445*, 136586. [CrossRef]
16. Zhang, J.-Y.; Xia, C.; Wang, H.-F.; Tang, C. Recent advances in electrocatalytic oxygen reduction for on-site hydrogen peroxide synthesis in acidic media. *J. Energy Chem.* **2022**, *67*, 432–450. [CrossRef]
17. Zhang, C.; Shen, W.; Guo, K.; Xiong, M.; Zhang, J.; Lu, X. A Pentagonal Defect-Rich Metal-Free Carbon Electrocatalyst for Boosting Acidic O_2 Reduction to H_2O_2 Production. *J. Am. Chem. Soc.* **2023**, *145*, 11589–11598. [CrossRef] [PubMed]
18. Huang, X.; Zhang, J.; Luo, G.; Wang, D. Cobalt atoms anchored on nitrogen-doped hollow carbon spheres for efficient electrocatalysis of oxygen reduction to H_2O_2. *J. Phys. Energy* **2023**, *5*, 025001. [CrossRef]
19. Cui, X.; Zhong, L.; Zhao, X.; Xie, J.; He, D.; Yang, X.; Lin, K.; Wang, H.; Niu, L. Ultrafine Co nanoparticles confined in nitrogen-doped carbon toward two-electron oxygen reduction reaction for H_2O_2 electrosynthesis in acidic media. *Chin. Chem. Lett.* **2023**, *34*, 108291. [CrossRef]
20. Sui, W.; Li, W.; Zhang, Z.; Wu, W.; Xu, Z.; Wang, Y. Efficient and durable electrochemical oxygen reduction to H_2O_2 in acidic media assisted through catalyst layer design. *J. Power Sources* **2023**, *556*, 232438. [CrossRef]
21. Wang, X.; Liu, Y.; Liu, Z.; Li, Z.; Zhang, T.; Cheng, Y.; Lei, L.; Yang, B.; Hou, Y. Highly efficient electrosynthesis of H_2O_2 in acidic electrolyte on metal-free heteroatoms co-doped carbon nanosheets and simultaneously promoting Fenton process. *Chin. Chem. Lett.* **2024**, *35*, 108926. [CrossRef]
22. Deng, Z.; Mostaghimi, A.H.B.; Gong, M.; Chen, N.; Siahrostami, S.; Wang, X. Pd 4d Orbital Overlapping Modulation on Au@Pd Nanowires for Efficient H_2O_2 Production. *J. Am. Chem. Soc.* **2024**, *146*, 2816–2823. [CrossRef] [PubMed]
23. Song, M.; Chen, M.; Zhang, C.; Zhang, J.; Liu, W.; Huang, X.; Li, J.; Feng, G.; Wang, D. Modulating the Oxygen Reduction Selectivity in Pt or Pd Chalcogenides via the Ensemble Effect and Electronic Effect. *ACS Appl. Mater. Interfaces* **2023**, *15*, 31375–31383. [CrossRef]
24. Li, H.; Wen, P.; Itanze, D.S.; Hood, Z.D.; Adhikari, S.; Lu, C.; Ma, X.; Dun, C.; Jiang, L.; Carroll, D.L.; et al. Scalable neutral H_2O_2 electrosynthesis by platinum diphosphide nanocrystals by regulating oxygen reduction reaction pathways. *Nat. Commun.* **2020**, *11*, 3928. [CrossRef] [PubMed]
25. Sun, X.; Zhu, X.; Wang, Y.; Li, Y. 1T′-$MoTe_2$ monolayer: A promising two-dimensional catalyst for the electrochemical production of hydrogen peroxide. *Chin. J. Catal.* **2022**, *43*, 1520–1526. [CrossRef]
26. Sheng, H.; Hermes, E.D.; Yang, X.; Ying, D.; Janes, A.N.; Li, W.; Schmidt, J.R.; Jin, S. Electrocatalytic Production of H_2O_2 by Selective Oxygen Reduction Using Earth-Abundant Cobalt Pyrite (CoS_2). *ACS Catal.* **2019**, *9*, 8433–8442. [CrossRef]
27. Yan, L.; Cheng, X.; Wang, Y.; Wang, Z.; Zheng, L.; Yan, Y.; Lu, Y.; Sun, S.; Qiu, W.; Chen, G. Exsolved Co_3O_4 with tunable oxygen vacancies for electrocatalytic H_2O_2 production. *Mater. Today Energy* **2022**, *24*, 100931. [CrossRef]
28. Han, C.-D.; Zhang, Y.-C.; Zhang, Q.; Wu, J.-T.; Gao, J.; Zou, J.-J.; Zhu, X.-D. $NaBH_4$-induced phase transition of $CoSe_2$ with abundant Se deficiency for acidic oxygen reduction to hydrogen peroxide. *Rare Metals* **2023**, *43*, 500–510. [CrossRef]
29. Sheng, H.; Janes, A.N.; Ross, R.D.; Kaiman, D.; Huang, J.; Song, B.; Schmidt, J.R.; Jin, S. Stable and selective electrosynthesis of hydrogen peroxide and the electro-Fenton process on $CoSe_2$ polymorph catalysts. *Energy Environ. Sci.* **2020**, *13*, 4189–4203. [CrossRef]
30. Wang, Y.N.; Han, C.D.; Ma, L.; Duan, T.G.; Du, Y.; Wu, J.T.; Zou, J.J.; Gao, J.; Zhu, X.D.; Zhang, Y.C. Recent Progress of Transition Metal Selenides for Electrochemical Oxygen Reduction to Hydrogen Peroxide: From Catalyst Design to Electrolyzers Application. *Small* **2024**, *21*, 2309448. [CrossRef]
31. Cao, W.; Shen, Q.; Men, D.; Ouyang, B.; Sun, Y.; Xu, K. Phase engineering of iron group transition metal selenides for water splitting. *Mat. Chem. Front.* **2023**, *7*, 4865–4879. [CrossRef]

32. Gong, Y.; Li, Y.; Li, Y.; Liu, M.; Bai, Y.; Wu, C. Metal Selenides Anode Materials for Sodium Ion Batteries: Synthesis, Modification, and Application. *Small* **2022**, *19*, 2206194. [CrossRef] [PubMed]
33. Sun, Q.; Xu, G.; Xiong, B.; Chen, L.; Shi, J. Anion-tuned nickel chalcogenides electrocatalysts for efficient 2e$^-$ ORR towards H_2O_2 production in acidic media. *Nano Res.* **2022**, *16*, 4729–4735. [CrossRef] [PubMed]
34. Yu, L.; Pang, X.; Tian, Z.; Wang, S.; Feng, L. Fe-doped $NiSe_2$ nanorods for enhanced urea electrolysis of hydrogen generation. *Electrochim. Acta* **2023**, *440*, 141724. [CrossRef]
35. Fan, S.; Li, G.; Yang, G.; Guo, X.; Niu, X. $NiSe_2$ nanooctahedra as anodes for high-performance sodium-ion batteries. *New J. Chem.* **2019**, *43*, 12858–12864. [CrossRef]
36. Zhang, L.; Liang, J.; Yue, L.; Dong, K.; Xu, Z.; Li, T.; Liu, Q.; Luo, Y.; Liu, Y.; Gao, S.; et al. CoTe nanoparticle-embedded N-doped hollow carbon polyhedron: An efficient catalyst for H_2O_2 electrosynthesis in acidic media. *J. Mater. Chem. A* **2021**, *9*, 21703–21707. [CrossRef]
37. Zhang, L.; Liang, J.; Yue, L.; Xu, Z.; Dong, K.; Liu, Q.; Luo, Y.; Li, T.; Cheng, X.; Cui, G.; et al. N-doped carbon nanotubes supported $CoSe_2$ nanoparticles: A highly efficient and stable catalyst for H_2O_2 electrosynthesis in acidic media. *Nano Res.* **2021**, *15*, 304–309. [CrossRef] [PubMed]
38. Xu, X.; Sun, H.; Jiang, S.P.; Shao, Z. Modulating metal–organic frameworks for catalyzing acidic oxygen evolution for proton exchange membrane water electrolysis. *SusMat* **2021**, *1*, 460–481. [CrossRef]
39. Guo, R.; Shi, W.; Liu, W.; Yang, X.; Xie, Y.; Yang, T.; Xiao, J. Ultralow noble metals doping enables metal-organic framework derived $Ni(OH)_2$ nanocages as efficient water oxidation electrocatalysts. *Chem. Eng. J.* **2022**, *429*, 132478. [CrossRef]
40. Qu, J.; Bai, Y.; Li, X.; Song, K.; Zhang, S.; Wang, X.; Wang, X.; Dai, S. Rational design of $NiSe_2$@rGO nanocomposites for advanced hybrid supercapacitors. *J. Mater. Res. Technol. JMRT* **2021**, *15*, 6155–6161. [CrossRef]
41. Bai, J.; Ge, W.; Zhou, P.; Xu, P.; Wang, L.; Zhang, J.; Jiang, X.; Li, X.; Zhou, Q.; Deng, Y. Precise constructed atomically dispersed Fe/Ni sites on porous nitrogen-doped carbon for oxygen reduction. *J. Colloid Interface Sci.* **2022**, *616*, 433–439. [CrossRef] [PubMed]
42. Chen, W.-C.; Yang, G.; Zhao, Y.; Yuan, G.-Q.; Ye, J.-S.; Liu, H.-Y.; Xiao, X.-Y. Porous carbon polyhedrons with exclusive Metal-N_X moieties for efficient oxygen reduction reaction. *Int. J. Hydrogen Energy* **2021**, *46*, 39882–39891. [CrossRef]
43. Wu, Y.; Ge, L.; Veksha, A.; Lisak, G. Cobalt and nitrogen co-doped porous carbon/carbon nanotube hybrids anchored with nickel nanoparticles as high-performance electrocatalysts for oxygen reduction reactions. *Nanoscale* **2020**, *12*, 13028–13033. [CrossRef] [PubMed]
44. Long, Y.; Li, Q.; Zhang, Z.; Zeng, Q.; Liu, D.; Zhao, L.; Liu, Y.; Li, Y.; Zhang, Y.; Ji, K.; et al. Coupling $MoSe_2$ with Non-Stoichiometry $Ni_{0.85}Se$ in Carbon Hollow Nanoflowers for Efficient Electrocatalytic Synergistic Effect on Li-O_2 Batteries. *Small* **2023**, *20*, 2304882. [CrossRef] [PubMed]
45. Zhang, Y.; Yun, S.; Sun, M.; Wang, X.; Zhang, L.; Dang, J.; Yang, C.; Yang, J.; Dang, C.; Yuan, S. Implanted metal-nitrogen active sites enhance the electrocatalytic activity of zeolitic imidazolate zinc framework-derived porous carbon for the hydrogen evolution reaction in acidic and alkaline media. *J. Colloid Interface Sci.* **2021**, *604*, 441–457. [CrossRef] [PubMed]
46. Wang, H.; Wei, L.; Shen, J. Metal-free catalyst for efficient pH-universal oxygen reduction electrocatalysis in microbial fuel cell. *J. Electroanal. Chem.* **2022**, *911*, 116233. [CrossRef]
47. Liang, Z.; Tu, H.; Zhang, K.; Kong, Z.; Huang, M.; Xu, D.; Liu, S.; Wu, Y.; Hao, X. Self-supporting $NiSe_2$@BCNNTs electrode for High-Performance sodium ion batteries. *Chem. Eng. J.* **2022**, *437*, 135421. [CrossRef]
48. Xiao, X.; Ni, L.; Chen, G.; Ai, G.; Li, J.; Qiu, T.; Liu, X. Two-dimensional $NiSe_2$ nanosheets on carbon fiber cloth for high-performance lithium-ion batteries. *J. Alloy. Compd.* **2020**, *821*, 153218. [CrossRef]
49. Ding, L.; Zhao, J.; Bao, Z.; Zhang, S.; Shi, H.; Liu, J.; Wang, G.; Peng, X.; Zhong, X.; Wang, J. Synchronous generation of green oxidants H_2O_2 and O_3 by using a heterojunction bifunctional ZnO/ZnS@C electrocatalyst. *J. Mater. Chem. A* **2023**, *11*, 3454–3463. [CrossRef]
50. Mohamed, I.M.A.; Kanagaraj, P.; Yasin, A.S.; Iqbal, W.; Liu, C. Electrochemical impedance investigation of urea oxidation in alkaline media based on electrospun nanofibers towards the technology of direct-urea fuel cells. *J. Alloy. Compd.* **2020**, *816*, 152513. [CrossRef]
51. Hu, Y.; Zhang, J.; Shen, T.; Li, Z.; Chen, K.; Lu, Y.; Zhang, J.; Wang, D. Efficient Electrochemical Production of H_2O_2 on Hollow N-Doped Carbon Nanospheres with Abundant Micropores. *ACS Appl. Mater. Interfaces* **2021**, *13*, 29551–29557. [CrossRef] [PubMed]
52. Sun, Y.L.; Yue, M.F.; Chen, H.Q.; Ze, H.J.; Wang, Y.H.; Dong, J.C.; Tian, Z.Q.; Fang, P.P.; Li, J.F. Exploring the Effect of Pd on the Oxygen Reduction Performance of Pt by In Situ Raman Spectroscopy. *Anal. Chem.* **2022**, *94*, 4779–4786. [CrossRef] [PubMed]
53. Wang, Y.; Yang, H.; Liu, Z.; Yin, K.; Wang, Z.; Huang, H.; Liu, Y.; Kang, Z.; Chen, Z. Efficient hydrogen peroxide production enabled by exploring layered metal telluride as two electron oxygen reduction reaction electrocatalyst. *J. Energy Chem.* **2023**, *87*, 247–255. [CrossRef]
54. Jiang, C.; Fei, Y.-F.; Xu, W.; Bao, Z.; Shao, Y.; Zhang, S.; Hu, Z.-T.; Wang, J. Synergistic effects of Bi_2O_3 and Ta_2O_5 for efficient electrochemical production of H_2O_2. *Appl. Catal. B Environ.* **2023**, *334*, 122867. [CrossRef]
55. Wang, Y.M.; Huang, H.; Wu, J.; Yang, H.Y.; Kang, Z.H.; Liu, Y.; Wang, Z.W.; Menezes, P.W.; Chen, Z.L. Charge-Polarized Selenium Vacancy in Nickel Diselenide Enabling Efficient and Stable Electrocatalytic Conversion of Oxygen to Hydrogen Peroxide. *Adv. Sci.* **2023**, *10*, 10. [CrossRef] [PubMed]

56. Wu, J.; Hou, M.; Chen, Z.; Hao, W.; Pan, X.; Yang, H.; Cen, W.; Liu, Y.; Huang, H.; Menezes, P.W.; et al. Composition Engineering of Amorphous Nickel Boride Nanoarchitectures Enabling Highly Efficient Electrosynthesis of Hydrogen Peroxide. *Adv. Mater.* **2022**, *34*, 2202995. [CrossRef] [PubMed]
57. Ross, R.D.; Sheng, H.; Parihar, A.; Huang, J.; Jin, S. Compositionally Tuned Trimetallic Thiospinel Catalysts for Enhanced Electrosynthesis of Hydrogen Peroxide and Built-In Hydroxyl Radical Generation. *ACS Catal.* **2021**, *11*, 12643–12650. [CrossRef]
58. Zhang, Y.; Jiang, H.; Zhang, C.; Feng, Y.; Feng, H.; Zhu, S.; Hu, J. High-efficiency oxygen reduction by late transition metal oxides to produce H_2O_2. *J. Mater. Chem. A* **2024**, *12*, 6123–6133. [CrossRef]
59. Xie, J.; Zhong, L.; Yang, X.; He, D.; Lin, K.; Chen, X.; Wang, H.; Gan, S.; Niu, L. Phosphorous and selenium tuning Co-based non-precious catalysts for electrosynthesis of H_2O_2 in acidic media. *Chin. Chem. Lett.* **2024**, *35*, 108472. [CrossRef]
60. Zheng, Y.R.; Hu, S.; Zhang, X.L.; Ju, H.; Wang, Z.; Tan, P.J.; Wu, R.; Gao, F.Y.; Zhuang, T.; Zheng, X.; et al. Black Phosphorous Mediates Surface Charge Redistribution of $CoSe_2$ for Electrochemical H_2O_2 Production in Acidic Electrolytes. *Adv. Mater.* **2022**, *34*, 2205414. [CrossRef]